Research Square

Preprints are preliminary reports that have not undergone peer review.
They should not be considered conclusive, used to inform clinical practice,
or referenced by the media as validated information.

Understanding simulated AMOC changes in single-forcing historical experiments

Domenico Giaquinto

domenico.giaquinto@cmcc.it

CMCC Foundation – Euro-Mediterranean Center on Climate Change

Dario Nicolì

CMCC Foundation – Euro-Mediterranean Center on Climate Change

Doug M. Smith

Met Office Hadley Centre

Doroteaciro Iovino

CMCC Foundation – Euro-Mediterranean Center on Climate Change

Dargan M. W. Frierson

University of Washington

Simona Masina

CMCC Foundation – Euro-Mediterranean Center on Climate Change

Panos J. Athanasiadis

CMCC Foundation – Euro-Mediterranean Center on Climate Change

Article

Keywords:

Posted Date: November 12th, 2026

DOI: https://doi.org/10.21203/rs.3.rs-11481945/v1

License: This work is licensed under a Creative Commons Attribution 4.0 International License.
Read Full License

Additional Declarations: No competing interests reported.

Understanding simulated AMOC changes in single-forcing historical experiments

Domenico Giaquinto[1*], Dario Nicolì[1], Doug M. Smith[2], Doroteaciro Iovino[1], Dargan M. W. Frierson[3], Simona Masina[1], Panos J. Athanasiadis[1]

[1]CMCC Foundation – Euro-Mediterranean Center on Climate Change, Bologna, Italy.
[2]Met Office Hadley Centre, Exeter, UK.
[3]Department of Atmospheric and Climate Science, University of Washington, Seattle, USA.

*Corresponding author(s). E-mail(s): domenico.giaquinto@cmcc.it;
Contributing authors: dario.nicoli@cmcc.it; doug.smith@metoffice.gov.uk;
dorotea.iovino@cmcc.it; dargan@uw.edu; simona.masina@cmcc.it;
panos.athanasiadis@cmcc.it;

Abstract

A potential forced Atlantic Meridional Overturning Circulation (AMOC) slowdown is widely debated, and its historical drivers and future evolution remain uncertain. Using a multi-model ensemble from the Large Ensemble Single Forcing Model Intercomparison Project, we assess model responses to greenhouse gases (GHGs) and anthropogenic aerosols (AAs) forcing, focusing on the AMOC and related processes in the high-latitude North Atlantic (NA). We find robust AMOC weakening under increasing GHGs and strengthening under increasing AAs, accompanied by largely antisymmetric spatial responses between GHGs-only and AAs-only simulations. Our results suggest that radiative forcing modifies Arctic sea-ice mass, leading to consistent changes in upper-ocean salinity over key deep-water formation regions. In turn, upper-ocean salinity and temperature modulate changes in upper-ocean density and stratification that contribute to the simulated AMOC trends. We discuss key mechanisms involved, including feedback mechanisms and the impacts of AMOC variations on the Subpolar NA. This study highlights the model responses to single external forcings on NA ocean processes, offering insights into model limitations in the representation of coupled processes that are essential for reliable climate projections.

Introduction

The Atlantic Meridional Overturning Circulation (AMOC) is a major component of the global ocean circulation, redistributing heat, freshwater, carbon, and nutrients [1–3]. The AMOC exerts its influence on (and is influenced by) multiple climate components, from the ocean to the atmosphere and the cryosphere [4, 5]. Temperature and salinity drive water sinking in the North Atlantic to the deep ocean and southward through buoyancy loss, while warm and salty near-surface waters move northward via the Gulf Stream [6, 7], which is key for the mean state European temperature and precipitation from sub-seasonal to decadal and longer timescales [8, 9]. Given its crucial role at the continental and global scale, various studies have investigated the possibility of AMOC weakening [10–13] or collapse [14, 15], using both observations, e.g. the Rapid Climate Change array at 26.5°N project [16, 17], and model simulations [18–21]. However, these scenarios remain uncertain, and further exploration of the relative consequences of such changes is needed [22–24], especially under the ongoing climate change.

External forcings may affect directly or indirectly key processes determining the state of the AMOC, with greenhouse gases (GHGs) and anthropogenic aerosols (AAs) being among the major radiative forcings to consider, given their different spatio-temporal effects [25].

Despite the accummulating evidence that increasing concentrations of GHGs are expected to weaken the AMOC [19, 26], whilst increasing concentrations of AAs tend to strengthen it [5, 27], the physical pathways linking radiative forcing to changes in deep-water formation and overturning strength remain incompletely understood. In particular, the relative roles of sea ice, upper-ocean salinity, temperature, and density in mediating the AMOC response have not yet been assessed consistently across a large multi-model ensemble. Consequently, the AMOC response to anthropogenic forcing remains one of the largest sources of uncertainty in future climate projections.

In a recent study, Nobre et al. [28] showed that a fast reduction in the AMOC in an abrupt-4xCO2 simulation in a coupled ocean–ice–atmosphere climate model is triggered by Arctic sea-ice melt reducing density in the NA through salinity depletion, and this impact was found to dominate over density changes induced by near-surface warming. Indeed, both salinity and temperature changes might affect the AMOC, though a salinity perturbation may cause a stronger AMOC change than a temperature perturbation [29]. Sévellec and co-authors [30] showed that while flux anomalies over the Subpolar North Atlantic (SPNA) impact the AMOC on decadal timescales, Arctic sea-ice decline explains the slowdown of the AMOC on

multidecadal timescales. Similarly, Liu et al. [31] simulated Arctic sea-ice loss by perturbing the radiative budget in a modeling experiment, and found that the associated AMOC weakening was induced by changes in both temperature and salinity. Many other studies report analogous mechanisms [19, 32, 33]. AMOC weakening subsequent to sea-ice reduction results in a decreased northward oceanic heat transport which contributes to reduced Arctic sea-ice loss [34], in a negative feedback loop between AMOC and sea ice. Liu et al. [35] quantified that a weakened AMOC can prevent more than 50% of Arctic sea-ice loss. It is therefore important to distinguish between internally generated AMOC feedbacks and externally forced responses. While sea ice and the AMOC interact through coupled feedback mechanisms, anthropogenic radiative forcing acts as an external perturbation that can alter these interactions by modifying the surface buoyancy budget.

AMOC weakening due to buoyancy anomalies resulting from freshwater inputs driven by Arctic sea-ice decline has also been documented in paleoclimate studies [36, 37], e.g. following the melting of the Laurentide Ice Sheet during the early Holocene [38]. In turn, the AMOC response to freshwater inputs is also thought to be associated with North Atlantic warm and cold events. For instance, McManus et al. [39] showed that during some of the coldest deglacial intervals in the North Atlantic, the AMOC was almost or completely shut down, while strong regional warming events during deglaciation were concurrent with rapid accelerations of the meridional overturning circulation.

Robson et al. [29] found that models with stronger aerosol radiative forcing simulate a stronger AMOC increase and through investigating the mechanisms behind AMOC strengthening in the CMIP6 historical simulations (1850–1985), they highlighted the role of turbulent heat loss over the SPNA and feedback mechanisms. AMOC increase caused by increased aerosol concentrations has also been documented as a consequence of large volcanic eruptions [40–42]. Moreover, CMIP6 models simulate AMOC decline after the 1980s, when aerosol emissions reduction policies were put in place, whilst GHGs remained relatively unchanged [5, 43] or kept increasing, which further demonstrates the competing nature of these forcings on AMOC trends.

In order to disentangle and attribute the effects of GHG and AA emissions on simulated AMOC evolution, the set of model simulations designed and conducted in the framework of the Large Ensemble Single Forcing Model Intercomparison Project (LESFMIP) [44] appears to be quite promising. This activity is an extension of the previous Detection and Attribution Model Intercomparison Project (DAMIP) [45], requesting larger ensemble sizes under the CMIP6 framework. In particular, the AAs-only (hist-aer) and GHGs-only (hist-GHG) experiments consist of single forcing historical runs in which simulations are driven with changes only in the

radiative forcing of interest, while all other external forcings are kept constant at preindustrial levels. We employ state-of-the-art LESFMIP experiments using a multi-model perspective to better understand and compare the mechanisms behind AMOC trends under GHG and AA forcing, in line with and expanding the work of previous studies, which employ fewer models/members or different modeling protocols (e.g., abrupt-4xCO2, DAMIP, CMIP6 historical simulations) [5, 19, 28, 32]. We focus on the historical period 1850–2014 and explore hist-aer and hist-GHG experiments, together with CMIP6 historical simulations. Building on previously proposed mechanisms linking Arctic sea ice, upper-ocean density, and the AMOC, we investigate the presence of these processes in the single-forcing simulations, showing substantial antisymmetry in the oceanic responses between hist-GHG and hist-aer experiments. The key mechanisms underlying AMOC weakening and strengthening are assessed within a standardized experimental framework which is designed to attribute changes to individual radiative forcings. The multi-model large-ensemble framework allows for better extracting the forced response, highlighting the long-term impacts of the two external radiative forcings on AMOC. In light of the expected evolution of these external forcings, the results presented here can potentially help assess the likely future forced changes of the AMOC.

Different climate models may respond differently to the same external forcing because of differences in their mean state and parameterizations [46, 47]. We therefore focus our analysis on signals and mechanisms that are consistent across the analyzed multi-model/multi-member ensemble, while explicitly highlighting inter-model differences where they are robust and physically meaningful. Moreover, the correspondence between model simulations and the real evolution of the climate system should never be taken for granted, as discrepancies in the observed and simulated signals are possible [48]. Main sources of uncertainty include model errors, non-additivity of the responses to different drivers due to nonlinearities, errors in forcings, and the impacts of misrepresented processes (lack of model fidelity).

Results

Antisymmetry in the AMOC response to hist-GHG and hist-aer radiative forcings

The contrasting effects of AA and GHG emissions on the North Atlantic Ocean are characterized by assessing differences in the surface radiative budget between the LESFMIP experiments hist-GHG and hist-aer. It is worth mentioning that, while GHG concentrations have increased throughout the period 1850–2014, global AA emissions peaked in the 1980s and have mostly declined in Europe and North America

since then [49–51]. However, the long-term aerosol trend over the full 1850–2014 period remains positive because emissions increased during most of the historical record.

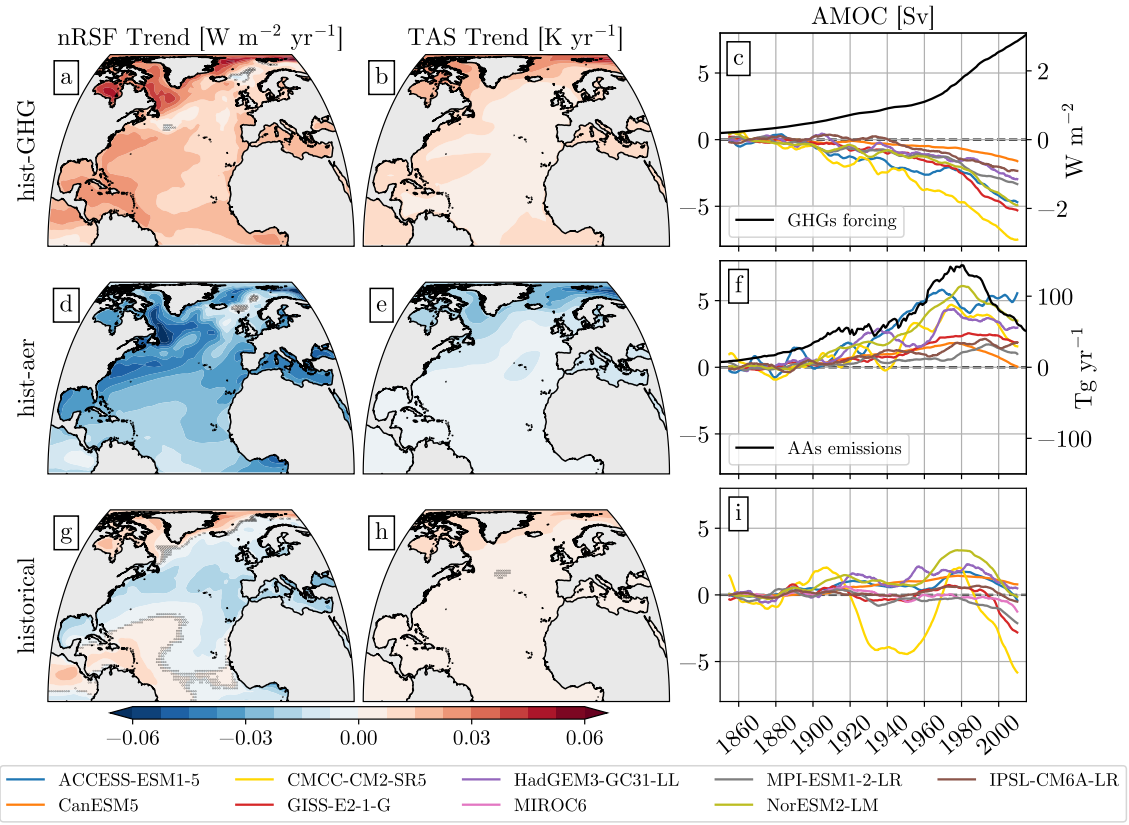


Fig. 1 Net radiative surface heat flux and AMOC evolution. Maps show the multi-model ensemble mean annual linear trends in 1850–2014 of nRSF (positive downward, left column), and near-surface temperature (TAS, middle column). Stippling indicates regions where the trend is not statistically significant at the 1% level (see Methods). The right column shows the ensemble-mean DJFM AMOC evolution in 1850–2014 for each of the analyzed models at 1250m depth and 45°N (colored solid lines, left y-axis). AMOC time series are smoothed with a 10-yr running mean. The black solid lines represent **c)** global GHG forcing (W m^{-2}) and **f)** North Atlantic AA emissions (Tg yr^{-1}) on the right y-axes. Hist-GHG experiment (top row), hist-aer experiment (middle row), and historical experiment (bottom row).

Figure 1a,d,g show the multi-model mean linear trend of the net surface radiative heat flux (nRSF, including both longwave and shortwave components) for the three analyzed experiments (hist-GHG, hist-aer, and historical) and for the entire year. The positive trend found for the hist-GHG experiment is in contrast with nRSF decrease in hist-aer. This sharp difference highlights both the contrasting radiative nature and spatial fingerprints of the two external forcings, which is also evident in near-surface air temperature trend (TAS, see Fig. 1b,e,h). Hist-GHG and hist-aer trends are found to be statistically significant (see Methods) almost everywhere, with few exceptions

over the Norwegian Sea (Fig. 1a,d). In hist-GHG, the increased downward longwave radiation causes near-surface warming (Fig. 1a,b); conversely, in the case of hist-aer, the general cooling of the lower troposphere (Fig. 1d,e) can be explained by two main processes: (*i*) the direct radiative effect, i.e. reflection of incoming shortwave radiation by aerosols back to space, also known as the dimming effect [52]; (*ii*) the indirect radiative effect related to the increased planetary albedo due to clouds responding to the increased AAs, known as the Twomey effect [53]. As for the historical experiment, the nRSF increases over the Arctic and the tropics and decreases over the mid-latitudes (Fig. 1g). On the other hand, the near-surface air temperature only exhibits areas of warming (Fig. 1h). It should be noted that the detected nRSF increase (decrease) in hist-GHG (hist-aer) and in the historical simulations over the Arctic region is not only due to the changes in the external forcing per se, but it is also and importantly enhanced by the positive sea-ice albedo feedback [54]. This is particularly evident in Fig. 1a,d, where the strongest nRSF trends are mainly found over sea-ice edge areas (Greenland, Barents, and Labrador seas, and Hudson Bay): in hist-GHG (hist-aer), the retreat (advance) of sea ice causes a considerable reduction (increase) of the surface albedo, enhancing (lowering) the absorbed radiative heat flux at the surface. The respective impacts of the different components of the nRSF, namely the longwave and shortwave components treated separately, as well as the corresponding downward and upward heat fluxes, are shown in Supplementary Fig. S2, where the influence of sea-ice changes on upward shortwave radiation appears more clearly. Given the indirect effect of aerosols on the incoming radiation via clouds, we also show the long-term changes of cloud fraction in Supplementary Fig. S3.

Figure 1c,f,i show AMOC anomaly time series defined as the ocean overturning mass streamfunction at 1250m depth and 45°N (colored solid lines); throughout the remainder of this study, references to the AMOC refer specifically to this one-dimensional index, unless otherwise specified. We also show the GHG forcing (black solid line in Fig. 1c) and AA emissions (black solid line in Fig. 1f). AMOC slowdown in hist-GHG is consistent with the global increase of GHG concentrations, whereas AMOC strengthening in hist-aer, which peaks around the 1980s, broadly follows the evolution of North Atlantic AA emissions in 1850–2014. As a result, the AMOC in the historical simulations does not exhibit a distinct long-term trend, until the peak of AAs emissions in the 1980s, after which a gradual AMOC decline is simulated by most models, consistent with the reduction of AA emissions ever since. The GHG forcing displayed by the black solid line in Fig. 1c comprises the contribution of CO_2, CH_4, N_2O, and chlorofluorocarbons. As for the AA emissions, black carbon, organic carbon, and sulfur dioxide were considered. Both GHG concentrations and AA emissions are obtained from the Community Emissions Data System [55]. While

GHGs are prescribed as spatially well-mixed in the models, AAs are prescribed with a spatially heterogeneous distribution, as shown in Supplementary Fig. S4. Historical simulations are characterized by a noticeable multi-decadal variability, with the CMCC-CM2-SR5 model being the one exhibiting the largest variations (yellow line in Fig. 1i). This behavior has also been documented by Terhaar et al. [56], who showed similar oscillations in air-sea heat flux and northward ocean heat transport (see their Fig. 5).

Overall, the dominant feature emerging from Fig. 1 is the pronounced antisymmetry between the hist-GHG and hist-aer responses in the nRSF, TAS and AMOC, with strong inter-model agreement. Moreover, the simulated AMOC evolution is robust to different choices of depth and latitude used to define the AMOC index, as shown in Supplementary Fig. S5.

Sea ice–salinity relationship and AMOC–salinity feedback

Near-surface warming associated with increased net surface radiative heat flux in hist-GHG (Fig. 1a,b) impacts sea-ice mass in the Arctic region, with a substantial reduction of sea ice in the extended winter season (DJFM) over 1850–2014 (Fig. 2a). The opposite applies for hist-aer, with increased sea ice in winter (Fig. 2b). These changes, i.e., sea-ice mass winter decrease in hist-GHG and increase in hist-aer, occur in the same direction in all other seasons (results not shown). In the historical simulations, the impacts of GHGs seem to dominate, resulting in a negative sea-ice mass trend (Fig. 2c), whose magnitude is weaker than the one in hist-GHG, being damped by AAs.

Figure 2d shows upper-ocean salinity trends against sea-ice mass trends over the climatological sea-ice region (see Methods). The upper-ocean is defined here as the ocean layer extending down to 500m depth. First, the trends positively correlate, as indicated by the overall alignment of the individual members (small dots in Fig. 2d), with sea-ice mass increases corresponding to salinity increases; second, the ensemble means of hist-aer experiments (triangle markers) all show increasing sea ice and salinity (upper-right quadrant) and are well separated from the ensemble means of hist-GHG experiment (diamond markers), which all correspond to decreasing sea ice and salinity (lower-left quadrant); finally, historical simulations lie between these two extremes (circle markers) and are closer to the hist-GHG region of the graph, showcasing the opposing effects of GHGs and AAs, and the prevailing nature of the former at high latitudes.

Figure 2 demonstrates that the primary mechanism behind the sea-ice and salinity relationship is fairly similar across the analyzed models, i.e., when sea ice melts,

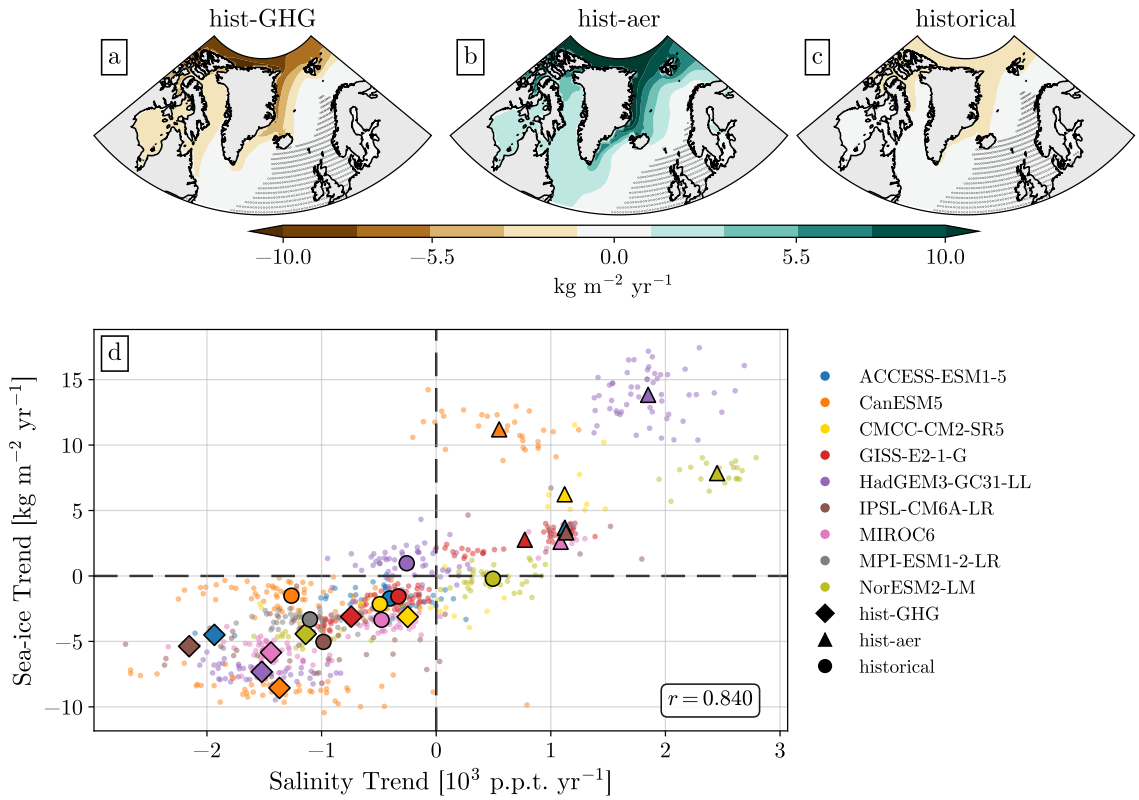


Fig. 2 Sea ice and salinity trend in 1850–2014. Maps show the DJFM multi-model mean linear trends in 1850–2014 of sea-ice mass for **a)** hist-GHG, **b)** hist-aer, and **c)** historical experiments. Stippling indicates regions where the trend is not statistically significant at the 1% level (see Methods). **d)** Scatter plot of sea-ice and salinity trends during DJFM 1850–2014 in the climatological sea-ice region (see Methods). Small dots represent individual members, while markers are ensemble means for each model for hist-GHG (diamonds), hist-aer (triangles), and historical experiments (circles). The Pearson's r correlation in the box refers to individual members.

freshwater is injected into the ocean, causing salinity to decrease, whilst sea ice formation is associated with a negative freshwater flux, which causes salinity to rise. This applies over the region where sea ice is present (in the climatological sense), and it is not only true for the DJFM average linear trend, but also in terms of sea ice and salinity co-variability during the entire year, as shown in Supplementary Fig. S6.

High-latitude NA upper-ocean salinity and the AMOC are closely related, being tied in a positive feedback mechanism: the upper limb of the AMOC transports relatively saline subtropical waters toward the subpolar North Atlantic, contributing to the maintenance of upper-ocean salinity and density in deep-water formation regions, thereby favouring deep convection and a stronger overturning circulation [29]. On the other hand, the poleward heat transport associated with the AMOC constitutes a competing negative feedback, as the tropical surface warm waters transported northward by the AMOC tend to reduce upper-ocean density in the SPNA, damping deep convection and thereby AMOC strength. Thus, given the salinity-mediated

positive feedback, the analysed simulations are expected to exhibit a positive relationship between upper-ocean salinity and AMOC strength. Figure 3 shows scatter plots of AMOC and salinity trends for four different high-latitude regions; it confirms that this relationship is robust across the different high-latitude regions considered. Despite some minor differences, the overall picture is consistent across the

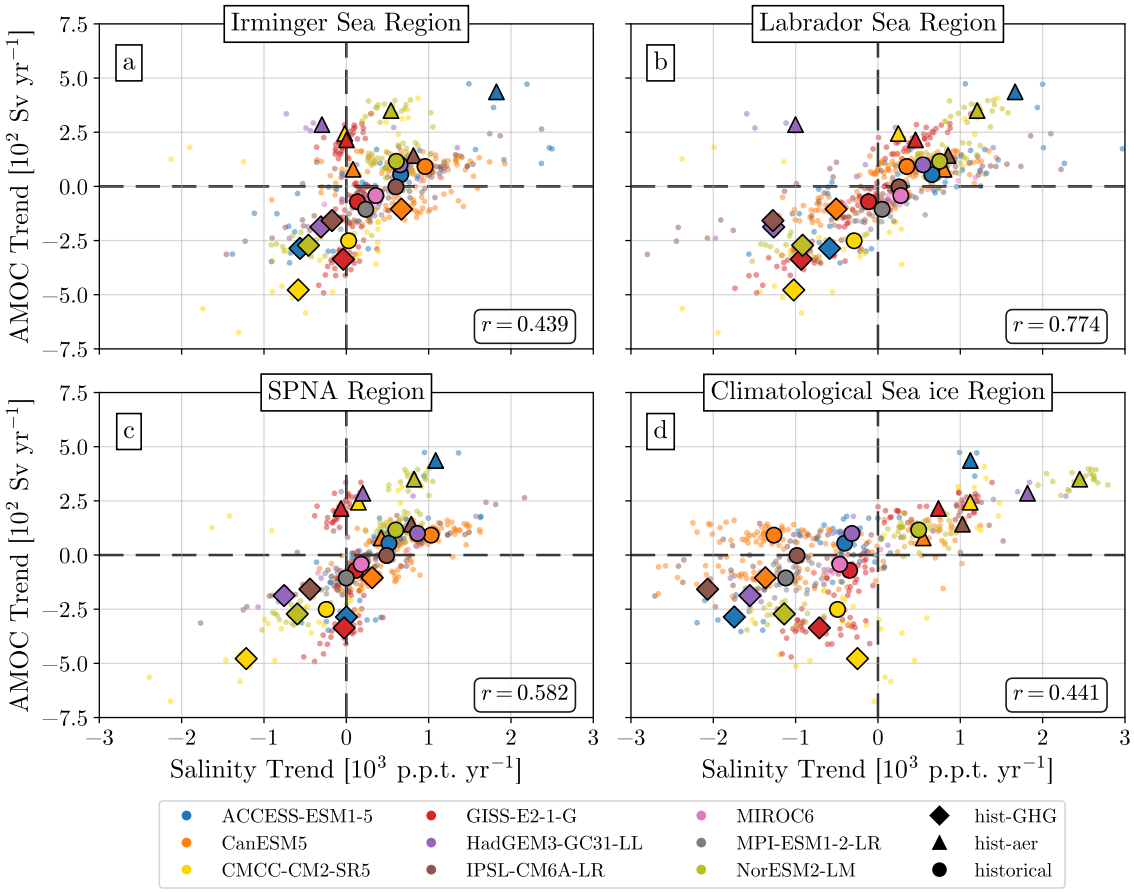


Fig. 3 AMOC and salinity trends in 1850–2014. Scatter plots of AMOC and salinity trends during DJFM 1850–2014. Salinity trend is computed by averaging over **a)** the Irminger Sea region, **b)** the Labrador Sea region, **c)** the SPNA region, and **d)** the climatological sea-ice region (see Methods). Small dots represent individual members, while markers are ensemble means for each model for hist-GHG (diamonds), hist-aer (triangles), and historical experiments (circles). Pearson's r correlation values in the boxes refer to individual members.

different areas: the AMOC and salinity are characterized by a positive correlation and, most importantly, while AMOC weakening in hist-GHG corresponds to salinity decrease (diamond markers), AMOC strengthening in hist-aer is accompanied by salinity increase (triangle markers), with historical experiments (circle markers) lying between hist-GHG and hist-aer.

Disentangling the respective roles of the AMOC and salinity as drivers or responses remains challenging due to the positive feedback mechanism they are

involved in. While it is well established that the AMOC both responds to and influences salinity, our results suggest that the externally forced sea ice changes may be a considerable source of upper-ocean salinity trends in these experiments. These trends appear to be largely controlled by radiative forcing and characterized by variations which cannot be explained by the AMOC long-term trend. Further details on the relationship between upper-ocean salinity and temperature with the AMOC, including their respective roles as driving and/or driven processes, are provided in the discussion section.

AMOC trends and density variations in deep-water formation regions

The AMOC–salinity positive feedback cannot alone explain long-term AMOC trends (Fig. 1c,f), as the overturning circulation is ultimately driven by upper-ocean density changes over areas of deep-water formation, and thus both salinity and ocean temperature play a role. Therefore, we isolate the contributions of salinity and temperature variability to density changes, using a first-order decomposition of density variability into salinity-driven and temperature-driven components. Specifically, we call ρ the density calculated from the time-varying upper-ocean temperature and salinity fields, ρ_S the density computed with time-varying salinity and climatological mean temperature fields, and ρ_T the density computed with time-varying temperature and climatological mean salinity fields. We then compute the anomalies associated with each field and the respective temporal trends. The result is shown in Fig. 4.

Density decreases over time in hist-GHG (Fig. 4a), and it increases in hist-aer (Fig. 4d), while the long-term trend found in the historical simulations is mostly negligible (Fig. 4g). This is in line with AMOC evolution as depicted in Fig. 1c,f,i: AMOC weakening in hist-GHG is associated with density decrease, while AMOC strengthening in hist-aer is accompanied by density increase. Noticeably, in hist-GHG the SPNA shows a weaker negative trend compared to the rest of the NA (Fig. 4a), while in hist-aer the SPNA is the only region where the sign of the trend is negative, although negligible (Fig. 4d). The density variables ρ_S and ρ_T allow for assessing the relative influence of salinity and temperature changes on density. In the Arctic region, most of the density variations in wintertime are due to salinity in all three experiments, as upper-ocean temperature variations affect density less than salinity changes in cold and fresh environments (see Fig. 4c,f,i). At high latitudes, salinity and temperature variations have the same long-term impact on density, i.e., reducing the latter in hist-GHG and increasing it in hist-aer, with an important exception in the SPNA. Here,

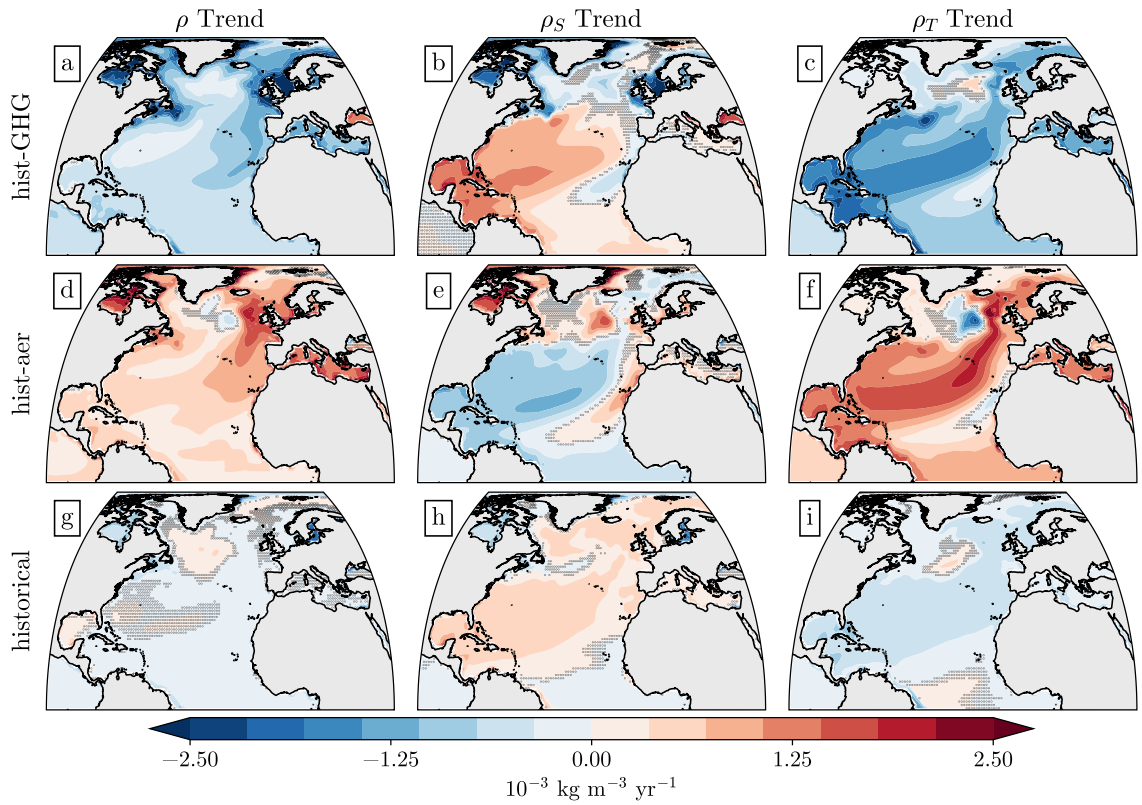


Fig. 4 Density trend in 1850–2014. Maps show the DJFM multi-model mean linear trends in the period 1850–2014 of upper-ocean density (left column), upper-ocean density computed with climatological upper-ocean temperature (middle column), and upper-ocean density computed with climatological upper-ocean salinity (right column). The upper-ocean is defined as the ocean layer extending down to 500m depth. Hist-GHG experiment (top row), hist-aer experiment (middle row), and historical experiment (bottom row). Stippling indicates regions where the trend is not statistically significant at the 1% level (see Methods).

salinity variations determine density decrease in hist-GHG (Fig. 4b), while temperature causes density increase over the so-called Warming Hole region (Fig. 4c). The opposite applies to hist-aer (see Fig. 4e,f). This explains the weak SPNA ρ trend signal found in hist-GHG (Fig. 4a), and the negative SPNA ρ trend found in hist-aer (Fig. 4d). Past studies have already partly attributed the presence of the Warming Hole to AMOC slowdown [13, 35, 57, 58], which seems to be the case in these experiments too. In particular, we show that not only does AMOC weakening cause less ocean warming in the SPNA compared with the rest of the NA, with consequent positive upper-ocean density anomaly trend (see Fig. 4c,i and Supplementary Fig. S7b,h), but also the opposite applies in the case of AMOC strengthening in hist-aer, where a "Cooling Hole" appears in the SPNA (see Fig. 4f and Supplementary Fig. S7e). Finally, at middle and low latitudes, salinity and temperature variations have opposite influences on density trends, with ρ being driven by ρ_T more than ρ_S, and

this is true for all three experiments. For a direct comparison between NA multi-model mean linear trend of upper-ocean salinity, temperature and density, please see Supplementary Fig. S7, where the Warming/Cooling Hole region clearly shows in the temperature maps. Finally, in order to quantify the relative influence of salinity and temperature on density, we perform a regression analysis of ρ onto ρ_T and ρ_S. We find that most models overestimate the impact of salinity on density at high latitudes compared to EN4 observations (for details, see Supplementary Fig. S8).

To directly connect AMOC variations to upper-ocean density, we now focus on those specific areas which are important for NA deep-water formation. We use mixed layer depth (MLD) as a proxy for deep convection, considering as key those regions where DJFM ensemble mean climatological MLD is high. The analyzed models have different high MLD regions, as depicted in Fig. 5. Although Fig. 5 refers to hist-

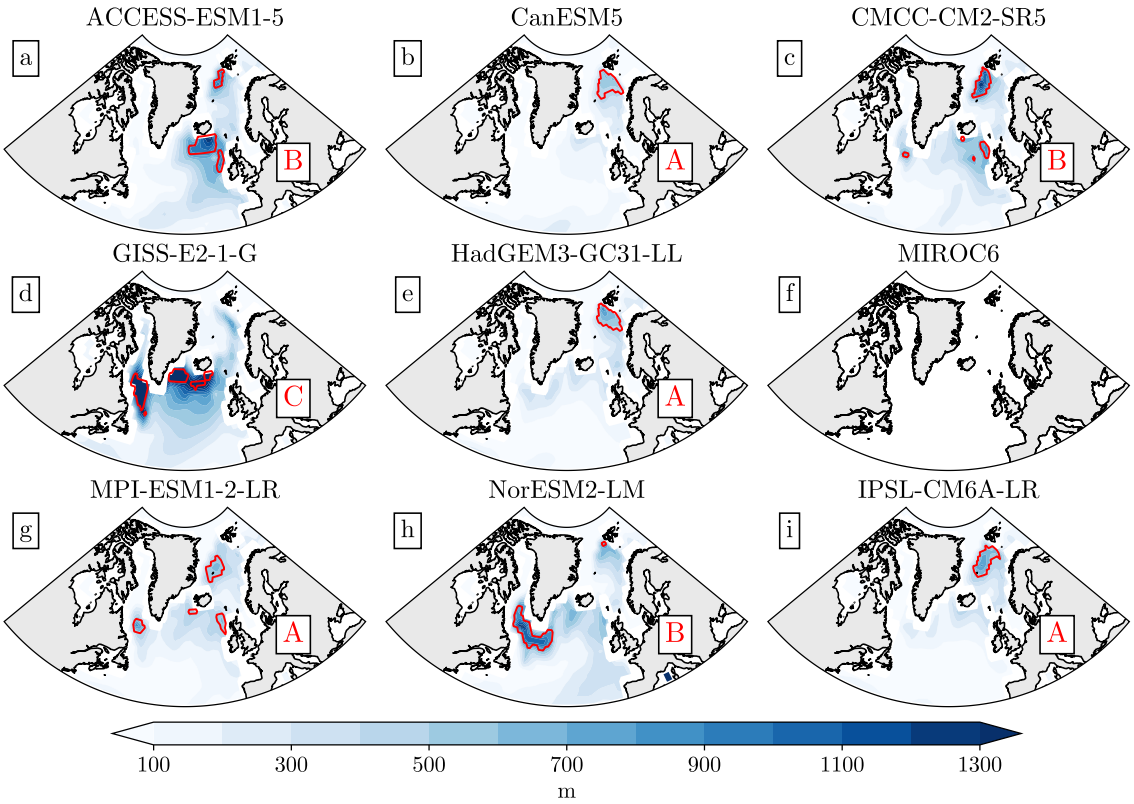


Fig. 5 Mixed layer depth climatology in 1850–2014. Maps show the hist-GHG DJFM ensemble mean 1850–2014 climatology of mixed layer depth for each model (MIROC6 data were not available). The red capital letters indicate the MLD group to which each model belongs based on the high MLD area (red contours).

GHG simulations only, the climatological MLD distribution is characteristic of the model configuration, with some small changes between the experiments, and thus the location of high MLD areas does not considerably change for hist-aer and historical runs (for details, see Supplementary Fig. S9). Except for MIROC6, for which no MLD

data were available, a first group of models (group A, see red capital letters in Fig. 5) includes those whose deep-water formation areas are almost exclusively located in the Greenland and Norwegian seas (CanESM5, HadGEM3-GC31-LL, MPI-ESM1-2-LR, and IPSL-CM6A-LR, see Fig. 5b,e,g,i), with a relatively shallow mixed layer. A second group (group B) comprises models whose MLD is higher in the Greenland and Norwegian seas and has substantial values in the SPNA too (ACCESS-ESM1-5, CMCC-CM2-SR5, and NorESM2-LM, see Fig. 5a,c,h). Finally, GISS-E2-1-G (Fig. 5d) stands out for having very large MLD values in the SPNA and negligible MLD in the Greenland and Norwegian seas (group C) compared to all other models. While the position of high MLD areas is not affected much by external forcings, MLD trends vary depending on GHG and AA evolution. We find that the trend over high MLD areas is mostly negative in hist-GHG and positive in hist-aer (see Supplementary Fig. S10), which is in line with upper-ocean density trends shown in Fig. 4a,d.

Each model–experiment pair is associated with a different high MLD area, which is identified by selecting those grid points poleward of 50°N for which the ensemble mean climatological MLD remains above the 97$^{\text{th}}$ percentile of the respective distribution for all the grid points in the NA (see red contours in Fig. 5). We then average the density trends over these grid points and compare them to the respective AMOC trends in Fig. 6. AMOC and density trends over high MLD areas posi-

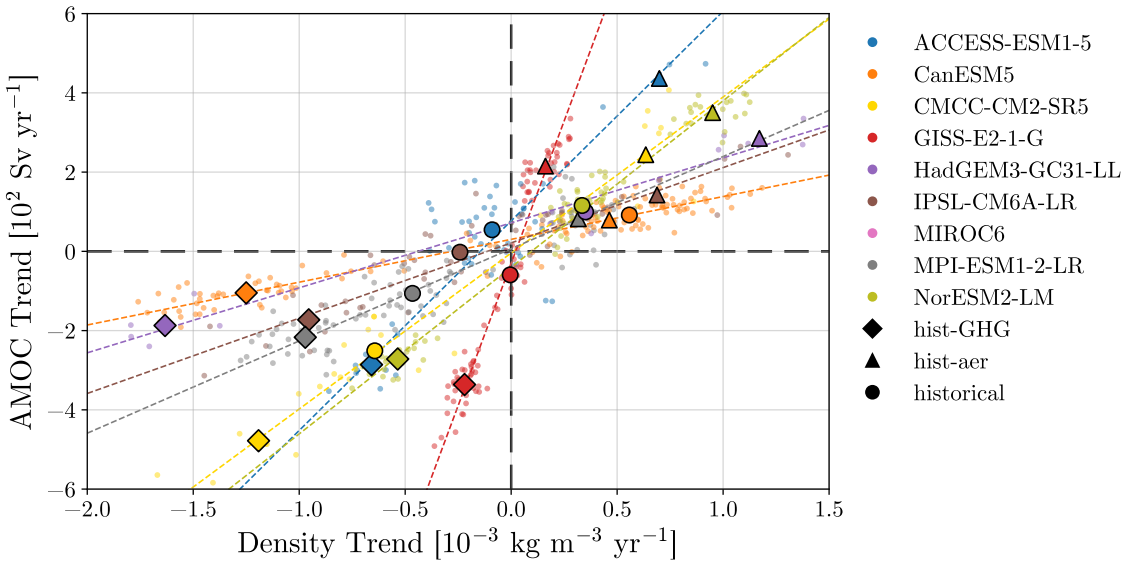


Fig. 6 AMOC and density trends in 1850–2014. Scatter plot of AMOC and density trends during DJFM 1850–2014. Density trends are computed by averaging over high climatological MLD areas, which are taken to be the same for each model–experiment pair. Small dots represent individual members, while markers indicate ensemble means for each model for hist-GHG (diamonds), hist-aer (triangles), and historical experiments (circles). Dashed lines indicate, for each model, a linear fit to the multi-experiment values of density and AMOC trends, considering all the respective individual simulations (small dots).

tively correlate, with hist-aer experiments showing increasing density associated with AMOC strengthening (triangle markers), hist-GHG experiments showing decreasing density and AMOC weakening (diamond markers), and historical experiments lying in between (circle markers). This result does not change for different choices of the threshold used to define high MLD area, as shown in Supplementary Fig. S11. Noticeably, the strength of the relationship between AMOC and upper-ocean density trends, which can be inferred from the linear interpolations in Fig. 6 (dashed lines), closely relates to the MLD climatology patterns described for Fig. 5: models belonging to group A have lower AMOC to density association (see Fig. 5b,e,g,i and orange, violet, gray, and brown dashed lines in Fig. 6). This interrelation increases for models belonging to group B (see Fig. 5a,c,h and blue, yellow, and green dashed lines in Fig. 6), and it is highest for GISS-E2-1-G (Fig. 5d and red dashed line in Fig. 6), which is characterized by large MLD values in the SPNA and negligible MLD in the Greenland and Norwegian seas compared to all other models.

Discussion

The Atlantic Meridional Overturning Circulation represents a key component of the Earth system, at both European and global scales. Understanding its main drivers and expected evolution remains crucial, especially in light of the ongoing climate change.

In this study, we disentangle the impacts of GHGs and AAs on simulated North Atlantic ocean processes connected to AMOC changes in the historical period using single-forcing multi-model large-ensemble experiments, with the aim of assessing the AMOC long-term forced response and associated mechanisms.

We argue that changes in the net radiative surface heat flux contribute to changes in sea-ice mass, initiating a sequence of changes in upper-ocean density, stratification, deep convection, and ultimately AMOC strength. Salinity and temperature both contribute to the detected density trends, with salinity supporting a positive feedback with the AMOC, and temperature partly offsetting it.

We show largely antisymmetric patterns in the long-term changes of various fields in hist-GHG compared to hist-aer, with the AMOC decreasing in hist-GHG and strengthening in hist-aer. Historical all-forcings simulations show a relatively stable AMOC anomaly, characterized by multidecadal oscillations in some models. AMOC multi-centennial oscillations have been associated with pulses of freshwater being released from Arctic sea ice and propagating towards deep-water formation sites [59, 60]. Although this would be consistent with the mechanisms we highlight here, Jiang et al. [60] only assess a preindustrial control simulation of IPSL-CM6A-LR,

and thus more specific studies are needed to confirm the relevance of this hypothesis across different models and timescales, even considering that historical simulations are more similar to preindustrial ones compared to single-forcing runs in terms of AMOC response, due to the opposing nature of GHGs and AAs.

The main variables and processes analyzed in the present study are illustrated in Fig. 7. The schematic summarizes the dominant relationships identified across

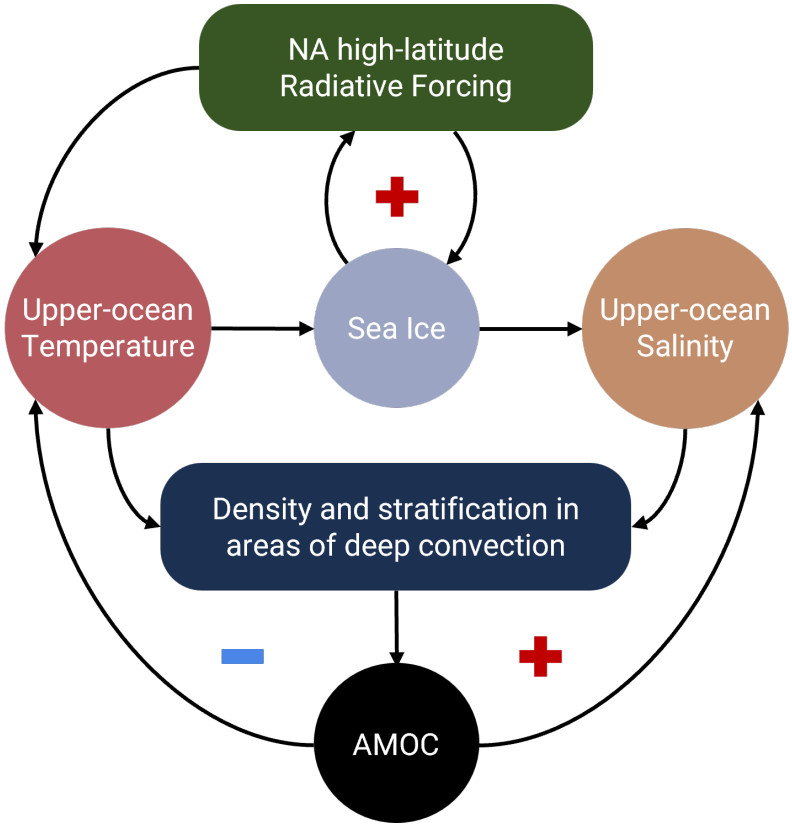


Fig. 7 Schematic of analyzed processes and their relationships. Arrows indicate direct relationships in the analyzed models and experiments between the processes connected. The red plus and blue minus signs indicate a positive and a negative feedback mechanism (loop), respectively.

the analyzed ensemble, and it is not intended as a comprehensive description of the AMOC system and all the connected processes in the NA, but rather to summarize the mechanisms described here. Its interpretation is limited to the single-forcing framework of the hist-GHG and hist-aer experiments. The external forcing due to GHGs and AAs at high latitudes in the NA (green box in Fig. 7) directly influences upper-ocean temperature and is also associated with changes in sea ice, which in turn induces a positive albedo feedback. Sea ice mediates changes in upper-ocean salinity which, together with changes in upper-ocean temperature, contribute to density variations in regions of deep convection. The AMOC responds to these changes, exhibiting a positive feedback with salinity and a negative feedback with temperature.

Arctic sea ice and the AMOC are closely linked [34], with the AMOC thought to be one of the primary drivers behind the cooling of the Northern Hemisphere and the associated warming of the Southern Hemisphere (i.e., the so-called thermal bipolar seesaw pattern) during the last ice age (see Zarriess et al. [61] and references within). Thus, in the absence of strong external forcing, the cause-effect relationship between Arctic sea ice and the AMOC could be bidirectional. This further supports that, in the simulations analyzed here, the AMOC is not the primary driving process, but instead it responds predominantly to externally forced changes in sea ice, salinity, and density: if the AMOC were the dominant driver, one would instead expect sea-ice increase in hist-GHG simulations, associated with AMOC weakening, and sea-ice decrease in hist-aer, associated with AMOC strengthening, as typically found in hosing experiments under pre-industrial control conditions [21, 62].

The negative feedback loop mediated by upper-ocean temperature, which connects AMOC weakening to North Atlantic ocean cooling, appears to be of secondary importance over the analyzed timescale relative to the effects of external forcings on sea ice and the consequent AMOC–salinity positive feedback. This likely reflects the continuous perturbation of the freshwater budget by the imposed radiative forcing, which persistently modifies sea-ice mass and upper-ocean salinity. By contrast, the temperature-mediated feedback mainly represents an internal adjustment of the circulation that acts to damp, rather than reverse, the externally forced response. A fingerprint of this negative feedback mechanism is also present in our simulations, where we show the presence of the Warming Hole in the subpolar region (see Fig. 4c,i and Supplementary Fig. S7b,h). Previous studies have already explained the Warming Hole in the SPNA with AMOC weakening [30, 58, 63]. Given its role in redistributing heat between the two hemispheres, AMOC weakening contrasts North Atlantic and Arctic warming under climate change [64] by reducing the northward ocean heat transport [65]. Additionally, we show that even under the cooling driven by anthropogenic aerosol concentrations (see Fig. 1d,e), the SPNA still features an area of opposite temperature trends compared with the rest of the NA (see Supplementary Fig. S7e), a "Cooling Hole", which also impacts upper-ocean density (see Fig. 4f), further demonstrating its connection to AMOC strength.

The freshening of the upper ocean and the subsequent weakening of deep-water formation driven by the externally forced Arctic sea-ice loss [13] is not the only mechanism that has been proposed to drive an AMOC slowdown. First of all, AMOC response in coupled ocean-ice-atmosphere models could be determined by the mean states of AMOC and sea ice, not only by the forcing itself. For instance, Weijer et al. [5] discuss the relationship between AMOC mean strength and its decline, also referring to other studies on the subject [26, 66], where models with weaker

AMOC have more Arctic sea ice and thus experience the strongest sea ice retreat and lower AMOC weakening under global warming. Second, the overturning circulation may also be affected by the interplay between the ocean and the atmosphere. For instance, Couldrey et al. [67] explore the weakening of the AMOC by perturbing the atmosphere–ocean fluxes of heat, freshwater and momentum under the FAFMIP protocol [68]. They show that most of the AMOC changes can be attributed to atmosphere–ocean heat fluxes more than freshwater and wind stress. Notably, this study does not account for changes in sea-ice—the perturbations are only applied to the sea-water surface, while the atmosphere and sea ice are not affected.

However, we expect turbulent heat fluxes to play a role in our simulations, especially over the SPNA, as also suggested by Robson et al. [29]. We find that over the SPNA the freshwater flux (i.e., the difference between precipitation and evaporation) and the turbulent heat fluxes contribute to density decrease in hist-GHG (increase in hist-aer), which is consistent with AMOC weakening (strengthening); at higher latitudes instead, especially where the sea-ice edge shifts, the contribution is opposite (see Supplementary Fig. S12). This suggests that freshwater and heat fluxes are more relevant for those models that feature areas of deep mixing in the SPNA, while upper-ocean density variations resulting from sea-ice changes are more important for those models with high MLD close to the sea-ice edge (group A, see Fig. 5). Further analysis is needed to quantify the respective impacts of the different density drivers; this would require a separate assessment for each model, which is beyond the scope of this study. The relationship between the AMOC and density described in Fig. 6 suggests that the SPNA is in principle the region that impacts the AMOC more strongly, which is also the reason why many of the studies exploring AMOC variability and long-term trend primarily focus on this area, attributing an important role to surface heat fluxes. Although this is expected to be the case in reality, we have shown that in some models (groups A and B, see Fig. 5) deep-water formation does not necessarily and solely occur in the SPNA, but also at higher latitudes, and thus sea ice plays an important role as well.

The correct representation of AMOC evolution and associated processes in CMIP6 models and its discrepancies with observations is highly debated in the literature, given the crucial role of the overturning circulation in the climate system [69]. For instance, Jackson et al. [70] show that AMOC mean state and weakening under increasing GHGs are stronger in the high-resolution version of HadGEM3-GC3.1, and these differences are motivated by the position of deep-water formation sites, with the western Subpolar gyre being more sensitive to CO_2 than the Greenland-Iceland-Norwegian seas. In another study, Li et al. [33] compare AMOC response to sea-ice loss in two models with different horizontal resolution, showing that the

higher-resolution configuration is characterized by lower AMOC weakening and subsequent full recovery. Other possible limitations of low-resolution models include the overestimation of the impact of salinity on density at high latitudes, as also shown in Fig. S8, and the consequent biased representation of the AMOC–salinity feedback mechanism [71, 72].

Finally, several studies have shown that AMOC slowdown can be followed by a recovery over longer timescales, even under increasing GHG concentrations [28, 73, 74]. In the absence of a complete AMOC shutdown, the salinity feedback could restore AMOC strength and reverse its decline [28], implying that the long-term evolution of the AMOC need not be monotonic.

Methods

Data

We use monthly data over 1850–2014 from the LESFMIP experiments hist-GHG (historical simulations with time-varying GHGs concentrations, while other forcings are kept constant at preindustrial levels) and hist-aer (historical simulations with time-varying AAs concentrations, while other forcings are kept constant at preindustrial levels) [44]. We also analyze the CMIP6 historical experiments, which include all time-varying external forcings [75]. Although LESFMIP experiments extend to 2020, the period 2015–2020 was excluded to ensure consistency with CMIP6 historical simulations, which terminate in 2014. LESFMIP data have been downloaded from the ESGF archive [76], as well as from the JASMIN platform [77], depending on availability. The analyzed models and associated references are listed in Table 1.

Model	Reference
ACCESS-ESM1-5	[78]
CanESM5	[79]
CMCC-CM2-SR5	[80]
GISS-E2-1-G	[81]
HadGEM3-GC31-LL	[82]
IPSL-CM6A-LR	[59]
MIROC6	[83]
MPI-ESM1-2-LR	[84]
NorESM2-LM	[85]

Table 1 Analyzed models in the present study and associated reference.

These models are all part of CMIP6 and they have all been evaluated in terms of historical-mean climate and variability, as reported for each one in the respective reference.

We also employ the ocean observational dataset EN.4.2.2 [86] using the correction scheme proposed by Gouretski et al. [87]. The results we present do not change using other types of bias correction, such as the ones proposed by Levitus et al. [88], Cowley et al. [89], or Cheng et al. [90] (not shown).

Regions and analyzed fields

We use data from the region 0-90°N and 100°W, 0°, mainly focusing on the North Atlantic (NA). More specifically, we analyze processes occurring over the Subpolar North Atlantic (SPNA), the Labrador Sea, the Irminger Sea, and the high-latitude NA region where sea ice is present in winter climatologies. While the former are fixed, the climatological sea-ice region is defined as the region where ensemble mean climatological sea-ice mass is above 200 kg m^{-2}, and thus it depends on the model, experiment and calendar season considered. Although this threshold has been arbitrarily defined, the main findings and conclusions of our study are not sensitive to this choice (results not shown). For further details about the regions and their specific location, please refer to Supplementary Fig. S1.

The AMOC is defined using CMIP6 variables *msftyz* (ocean y overturning mass streamfunction) and *msftmz* (ocean z overturning mass streamfunction), depending on output availability for each model, and it is expressed in Sverdrups (1 Sv = 10^6 m^3 s^{-1}). Other relevant ocean fields we use include sea-ice mass (*simass*, in kg m^{-2}), mixed layer depth (*mlotst*, in m), upper-ocean average salinity (*so*, in p.p.t.), and upper-ocean average temperature (*thetao*, in K). The upper ocean is defined as the ocean layer extending down to 500m depth. Additionally, we compute the average upper-ocean density (ρ, in kg m^{-3}), using the GSW python library [91].

Surface atmosphere heat fluxes are expressed in W m^{-2}, and the following components are employed: the downward latent surface heat flux (*hfls*), the downward sensible surface heat flux (*hfss*), the downward longwave radiative surface heat flux (*rlds*), the upward longwave radiative surface heat flux (*rlus*), the downward shortwave radiative surface heat flux (*rsds*), and the upward shortwave radiative surface heat flux (*rsus*). Moreover, we call net Radiative Surface Heat Flux (nRSF, positive downward) the algebraic sum of *rlds*, *rlus*, *rsds*, and *rsus*. Instead of providing both the downward and upward components, some models directly output the radiative net long- and shortwave heat fluxes, i.e. *rls* and *rss*, respectively. The latent surface heat flux *hfls* is used to compute the evaporation flux (E, in mm/mon) using the latent heat of vaporization $\lambda = 2.501 \times 10^6$ J kg^{-1}, assumed constant. Together with

precipitation (Pr, in mm mon^{-1}), the evaporation is used to define the freshwater flux $Pr-E$. We also employ the near-surface air temperature (TAS, in K).

All used monthly fields are remapped to a common regular 1° × 1° lat-lon grid via bilinear interpolation, using Climate Data Operators [92], and, unless otherwise specified, we use monthly anomalies relative to 1851–1890.

The ensemble size (number of members) used for each variables differed, subject to data availability at the time of completing this study. The respective ensemble sizes per variable, model, and experiment are reported in Supplementary Table S1. Although assessing the realism of the used models is out of the scope of the present work, comparisons between simulated and observed upper-ocean salinity, upper-ocean temperature and the AMOC climatologies are reported in Supplementary Figures S13, S14, and S15, as these variables are considered key for this study. AMOC observational data are taken from the RAPID AMOC project [93]. These comparisons are performed comparing historical runs against observation, since hist-GHG and hist-aer experiments are not directly comparable to the observed climate system.

Evolution of analyzed fields

The evolution of relevant processes over 1850–2014 is assessed either by analyzing one-dimensional time series averaged over a specific spatial region of interest, or by looking at the spatial distribution of linear trend coefficients over the NA for the process of interest.

Let $y_{m,n}(t,i)$ denote a variable that depends on time t and location i, from model m and member n. The linear trend $b_{m,n}(i)$ is defined as follows:

$$y_{m,n}(t,i) = a_{m,n}(i) + b_{m,n}(i) \cdot t + \epsilon_{m,n}(i), \tag{1}$$

and is estimated using least squares linear regression. The multi-model mean linear trend $b(i)$ is computed by averaging over all members of all models, so that each member has equal weight:

$$b(i) = \frac{1}{\sum_{m=1}^{M} N_m} \sum_{m=1}^{M} \left(\sum_{n=1}^{N_m} b_{m,n}(i) \right), \tag{2}$$

where M is the number of models and N_m the number of members of model m. The results are robust even when each model, rather than each member, is given equal weight.

Statistical significance of the multi-model mean linear trend $b(i)$ is assessed using a nonparametric bootstrap method, resampling $b_{m,n}(i)$ 1000 times with replacement.

$b(i)$ is considered significant at the 1% level when 0 lies outside the 0.5th–99.5th percentile range of the resampled $b_{m,n}(i)$ distribution.

Data Availability

All data used in this study are publicly available. CMIP6 LESFMIP simulations can be downloaded from the ESGF archive at https://esgf.github.io/.

EN.4.2.2 observations can be obtained from https://www.metoffice.gov.uk/hadobs/en4/ and are © British Crown Copyright, Met Office, 2026, provided under a Non-Commercial Government Licence http://www.nationalarchives.gov.uk/doc/non-commercial-government-licence/version/2/.

Data from the RAPID AMOC observing project is funded by the Natural Environment Research Council, U.S. National Science Foundation (NSF) with support from NOAA. They are freely available from https://rapid.ac.uk/.

Code availability

The code used for this study is not publicly available but may be made available on reasonable request from the corresponding author.

References

[1] Wunsch, C. What is the thermohaline circulation? *Science* **298**, 1179–1181 (2002).

[2] Gordon, A. L. Interocean exchange of thermocline water. *Journal of Geophysical Research: Oceans* **91**, 5037–5046 (1986).

[3] Stommel, H. & Arons, A. On the abyssal circulation of the world ocean — ii. an idealized model of the circulation pattern and amplitude in oceanic basins. *Deep Sea Research (1953)* **6**, 217–233 (1959).

[4] Zhang, R. Mechanisms for low-frequency variability of summer arctic sea ice extent. *Proceedings of the National Academy of Sciences* **112**, 4570–4575 (2015).

[5] Weijer, W., Cheng, W., Garuba, O. A., Hu, A. & Nadiga, B. T. Cmip6 models predict significant 21st century decline of the atlantic meridional overturning circulation. *Geophysical Research Letters* **47** (2020).

[6] Johns, W. E. *et al.* Continuous, array-based estimates of atlantic ocean heat transport at 26.5°n. *Journal of Climate* **24**, 2429–2449 (2011).

[7] Buckley, M. W. & Marshall, J. Observations, inferences, and mechanisms of the atlantic meridional overturning circulation: A review. *Reviews of Geophysics* **54**, 5–63 (2016).

[8] Vacca, A. V., Bellomo, K., Fabiano, F. & von Hardenberg, J. On the role of amoc weakening in shaping wintertime euro-atlantic atmospheric circulation. *Climate Dynamics* **63** (2025).

[9] Palter, J. B. The role of the gulf stream in european climate. *Annual Review of Marine Science* **7**, 113–137 (2015).

[10] Solomon, S. *et al.* (eds) *Climate Change 2007: The Physical Science Basis. Contribution of Working Group I to the Fourth Assessment Report of the Intergovernmental Panel on Climate Change* (Cambridge University Press, Cambridge, United Kingdom and New York, NY, USA, 2007).

[11] Seidov, D., Mishonov, A. & Reagan, J. Amoc and north atlantic ocean decadal variability: A review. *Oceans* **6**, 59 (2025).

[12] Caesar, L., Rahmstorf, S. & Feulner, G. On the relationship between atlantic meridional overturning circulation slowdown and global surface warming. *Environmental Research Letters* **15**, 024003 (2020).

[13] Rahmstorf, S. *et al.* Exceptional twentieth-century slowdown in atlantic ocean overturning circulation. *Nature Climate Change* **5**, 475–480 (2015).

[14] Boers, N. Observation-based early-warning signals for a collapse of the atlantic meridional overturning circulation. *Nature Climate Change* **11**, 680–688 (2021).

[15] Hawkins, E. *et al.* Bistability of the atlantic overturning circulation in a global climate model and links to ocean freshwater transport: Bistability of the atlantic moc. *Geophysical Research Letters* **38** (2011).

[16] Häkkinen, S. & Rhines, P. B. Decline of subpolar north atlantic circulation during the 1990s. *Science* **304**, 555–559 (2004).

[17] Smeed, D. A. *et al.* Observed decline of the atlantic meridional overturning circulation 2004–2012. *Ocean Science* **10**, 29–38 (2014).

[18] Cheng, W., Chiang, J. C. H. & Zhang, D. Atlantic meridional overturning circulation (amoc) in cmip5 models: Rcp and historical simulations. *Journal of*

Climate **26**, 7187–7197 (2013).

[19] Madan, G., Gjermundsen, A., Iversen, S. C. & LaCasce, J. H. The weakening amoc under extreme climate change. *Climate Dynamics* **62**, 1291–1309 (2023).

[20] Drijfhout, S., Angevaare, J. R., Mecking, J., van Westen, R. M. & Rahmstorf, S. Shutdown of northern atlantic overturning after 2100 following deep mixing collapse in cmip6 projections. *Environmental Research Letters* **20**, 094062 (2025).

[21] Bellomo, K. & Mehling, O. Impacts and state-dependence of amoc weakening in a warming climate. *Geophysical Research Letters* **51** (2024).

[22] Bellomo, K. *et al.* Impacts of a weakened amoc on precipitation over the euro-atlantic region in the ec-earth3 climate model. *Climate Dynamics* **61**, 3397–3416 (2023).

[23] Ma, Q. *et al.* Revisiting climate impacts of an amoc slowdown: dependence on freshwater locations in the north atlantic. *Science Advances* **10** (2024).

[24] Jackson, L. C. *et al.* Global and european climate impacts of a slowdown of the amoc in a high resolution gcm. *Climate Dynamics* **45**, 3299–3316 (2015).

[25] Xie, S.-P., Lu, B. & Xiang, B. Similar spatial patterns of climate responses to aerosol and greenhouse gas changes. *Nature Geoscience* **6**, 828–832 (2013).

[26] Rugenstein, M. A. A., Winton, M., Stouffer, R. J., Griffies, S. M. & Hallberg, R. Northern high-latitude heat budget decomposition and transient warming. *Journal of Climate* **26**, 609–621 (2013).

[27] Menary, M. B. *et al.* Mechanisms of aerosol-forced amoc variability in a state of the art climate model. *Journal of Geophysical Research: Oceans* **118**, 2087–2096 (2013).

[28] Nobre, P. *et al.* Amoc decline and recovery in a warmer climate. *Scientific Reports* **13** (2023).

[29] Robson, J. *et al.* The role of anthropogenic aerosol forcing in the 1850–1985 strengthening of the amoc in cmip6 historical simulations. *Journal of Climate* **35**, 3243–3263 (2022).

[30] Sévellec, F., Fedorov, A. V. & Liu, W. Arctic sea-ice decline weakens the atlantic meridional overturning circulation. *Nature Climate Change* **7**, 604–610 (2017).

[31] Liu, W., Fedorov, A. & Sévellec, F. The mechanisms of the atlantic meridional overturning circulation slowdown induced by arctic sea ice decline. *Journal of Climate* **32**, 977–996 (2019).

[32] Knutti, R., Flückiger, J., Stocker, T. F. & Timmermann, A. Strong hemispheric coupling of glacial climate through freshwater discharge and ocean circulation. *Nature* **430**, 851–856 (2004).

[33] Li, H., Fedorov, A. & Liu, W. Amoc stability and diverging response to arctic sea ice decline in two climate models. *Journal of Climate* 1–47 (2021).

[34] Liu, W. & Fedorov, A. Interaction between arctic sea ice and the atlantic meridional overturning circulation in a warming climate. *Climate Dynamics* **58**, 1811–1827 (2021).

[35] Liu, W., Fedorov, A. V., Xie, S.-P. & Hu, S. Climate impacts of a weakened atlantic meridional overturning circulation in a warming climate. *Science Advances* **6** (2020).

[36] Peltier, W. R., Vettoretti, G. & Stastna, M. Atlantic meridional overturning and climate response to arctic ocean freshening. *Geophysical Research Letters* **33** (2006).

[37] Liu, Z. *et al.* Transient simulation of last deglaciation with a new mechanism for bølling-allerød warming. *Science* **325**, 310–314 (2009).

[38] Bamberg, A. *et al.* Reduced north atlantic central water formation in response to early holocene ice-sheet melting. *Geophysical Research Letters* **37** (2010).

[39] McManus, J. F., Francois, R., Gherardi, J.-M., Keigwin, L. D. & Brown-Leger, S. Collapse and rapid resumption of atlantic meridional circulation linked to deglacial climate changes. *Nature* **428**, 834–837 (2004).

[40] Zhang, R. *et al.* A review of the role of the atlantic meridional overturning circulation in atlantic multidecadal variability and associated climate impacts. *Reviews of Geophysics* **57**, 316–375 (2019).

[41] Bilbao, R. *et al.* Impact of volcanic eruptions on cmip6 decadal predictions: a multi-model analysis. *Earth System Dynamics* **15**, 501–525 (2024).

[42] Chen, K. *et al.* Modulating and resetting impacts of different volcanic eruptions on north atlantic sst variations. *Journal of Geophysical Research: Atmospheres* **127** (2022).

[43] Delworth, T. L. & Dixon, K. W. Have anthropogenic aerosols delayed a greenhouse gas-induced weakening of the north atlantic thermohaline circulation? *Geophysical Research Letters* **33** (2006).

[44] Smith, D. M. *et al.* Attribution of multi-annual to decadal changes in the climate system: The large ensemble single forcing model intercomparison project (lesfmip). *Frontiers in Climate* **4** (2022).

[45] Gillett, N. P. *et al.* The detection and attribution model intercomparison project (damip v1.0) contribution to cmip6. *Geoscientific Model Development* **9**, 3685–3697 (2016).

[46] Smith, D. M. *et al.* North atlantic climate far more predictable than models imply. *Nature* **583**, 796–800 (2020).

[47] Smith, D. M. *et al.* Mitigation needed to avoid unprecedented multi-decadal north atlantic oscillation magnitude. *Nature Climate Change* **15**, 403–410 (2025).

[48] Simpson, I. R. *et al.* Confronting earth system model trends with observations. *Science Advances* **11** (2025).

[49] Lund, M. T., Myhre, G. & Samset, B. H. Anthropogenic aerosol forcing under the shared socioeconomic pathways. *Atmospheric Chemistry and Physics* **19**, 13827–13839 (2019).

[50] Hoesly, R. M. *et al.* Historical (1750–2014) anthropogenic emissions of reactive gases and aerosols from the community emissions data system (ceds). *Geoscientific Model Development* **11**, 369–408 (2018).

[51] Yang, Y., Lou, S., Wang, H., Wang, P. & Liao, H. Trends and source apportionment of aerosols in europe during 1980–2018. *Atmospheric Chemistry and Physics* **20**, 2579–2590 (2020).

[52] Wild, M. Global dimming and brightening: A review. *Journal of Geophysical Research: Atmospheres* **114** (2009).

[53] Lohmann, U. Aerosol effects on clouds and climate. *Space Science Reviews* **125**, 129–137 (2006).

[54] Perovich, D. K. & Polashenski, C. Albedo evolution of seasonal arctic sea ice. *Geophysical Research Letters* **39** (2012).

[55] Hoesly, R. & Smith, S. CEDS v_2024_04_01 Release Emission Data (2024). URL https://doi.org/10.5281/zenodo.10904361.

[56] Terhaar, J., Vogt, L. & Foukal, N. P. Atlantic overturning inferred from air-sea heat fluxes indicates no decline since the 1960s. *Nature Communications* **16** (2025).

[57] Sgubin, G., Swingedouw, D., Drijfhout, S., Mary, Y. & Bennabi, A. Abrupt cooling over the north atlantic in modern climate models. *Nature Communications* **8** (2017).

[58] Drijfhout, S., van Oldenborgh, G. J. & Cimatoribus, A. Is a decline of amoc causing the warming hole above the north atlantic in observed and modeled warming patterns? *Journal of Climate* **25**, 8373–8379 (2012).

[59] Boucher, O. *et al.* Presentation and evaluation of the ipsl-cm6a-lr climate model. *Journal of Advances in Modeling Earth Systems* **12** (2020).

[60] Jiang, W., Gastineau, G. & Codron, F. Multicentennial variability driven by salinity exchanges between the atlantic and the arctic ocean in a coupled climate model. *Journal of Advances in Modeling Earth Systems* **13** (2021).

[61] Zarriess, M. *et al.* Bipolar seesaw in the northeastern tropical atlantic during heinrich stadials. *Geophysical Research Letters* **38**, n/a–n/a (2011).

[62] Jackson, L. C. *et al.* Understanding amoc stability: the north atlantic hosing model intercomparison project. *Geoscientific Model Development* **16**, 1975–1995 (2023).

[63] Caesar, L., Rahmstorf, S., Robinson, A., Feulner, G. & Saba, V. Observed fingerprint of a weakening atlantic ocean overturning circulation. *Nature* **556**, 191–196 (2018).

[64] Hahn, L. C. *et al.* Large uncertainty in arctic warming driven by the atlantic meridional overturning circulation. *Geophysical Research Letters* **52** (2025).

[65] Mecking, J. V. & Drijfhout, S. S. The decrease in ocean heat transport in response to global warming. *Nature Climate Change* **13**, 1229–1236 (2023).

[66] Levermann, A., Mignot, J., Nawrath, S. & Rahmstorf, S. The role of northern sea ice cover for the weakening of the thermohaline circulation under global warming. *Journal of Climate* **20**, 4160–4171 (2007).

[67] Couldrey, M. P. *et al.* Greenhouse-gas forced changes in the atlantic meridional overturning circulation and related worldwide sea-level change. *Climate Dynamics* **60**, 2003–2039 (2022).

[68] Gregory, J. M. *et al.* The flux-anomaly-forced model intercomparison project (fafmip) contribution to cmip6: investigation of sea-level and ocean climate change in response to co_2 forcing. *Geoscientific Model Development* **9**, 3993–4017 (2016).

[69] McCarthy, G. D. & Caesar, L. Can we trust projections of amoc weakening based on climate models that cannot reproduce the past? *Philosophical Transactions of the Royal Society A: Mathematical, Physical and Engineering Sciences* **381** (2023).

[70] Jackson, L. C. *et al.* Impact of ocean resolution and mean state on the rate of amoc weakening. *Climate Dynamics* **55**, 1711–1732 (2020).

[71] Patrizio, C. R. *et al.* Improved extratropical north atlantic atmosphere–ocean variability with increasing ocean model resolution. *Journal of Climate* **36**, 8403–8424 (2023).

[72] Reintges, A., Robson, J. I., Sutton, R. & Yeager, S. G. Subpolar north atlantic mean state affects the response of the atlantic meridional overturning circulation to the north atlantic oscillation in cmip6 models. *Journal of Climate* **37**, 5543–5559 (2024).

[73] Curtis, P. E. & Fedorov, A. V. Collapse and slow recovery of the atlantic meridional overturning circulation (amoc) under abrupt greenhouse gas forcing. *Climate Dynamics* (2024).

[74] Ackermann, L., Danek, C., Gierz, P. & Lohmann, G. Amoc recovery in a multicentennial scenario using a coupled atmosphere-ocean-ice sheet model. *Geophysical Research Letters* **47** (2020).

[75] Eyring, V. *et al.* Overview of the coupled model intercomparison project phase 6 (cmip6) experimental design and organization. *Geoscientific Model Development* **9**, 1937–1958 (2016).

[76] Cinquini, L. *et al.* The earth system grid federation: An open infrastructure for access to distributed geospatial data. *Future Generation Computer Systems* **36**, 400–417 (2014).

[77] Lawrence, B. N. *et al.* Storing and manipulating environmental big data with jasmin. *2013 IEEE international conference on big data* 68–75 (2013).

[78] Ziehn, T. *et al.* The australian earth system model: Access-esm1.5. *Journal of Southern Hemisphere Earth Systems Science* **70**, 193–214 (2020).

[79] Swart, N. C. *et al.* The canadian earth system model version 5 (canesm5.0.3). *Geoscientific Model Development* **12**, 4823–4873 (2019).

[80] Cherchi, A. *et al.* Global mean climate and main patterns of variability in the cmcc-cm2 coupled model. *Journal of Advances in Modeling Earth Systems* **11**, 185–209 (2019).

[81] Kelley, M. *et al.* Giss-e2.1: Configurations and climatology. *Journal of Advances in Modeling Earth Systems* **12** (2020).

[82] Williams, K. D. *et al.* The met office global coupled model 3.0 and 3.1 (gc3.0 and gc3.1) configurations. *Journal of Advances in Modeling Earth Systems* **10**, 357–380 (2018).

[83] Tatebe, H. *et al.* Description and basic evaluation of simulated mean state, internal variability, and climate sensitivity in miroc6. *Geoscientific Model Development* **12**, 2727–2765 (2019).

[84] Mauritsen, T. *et al.* Developments in the mpi-m earth system model version 1.2 (mpi-esm1.2) and its response to increasing co2. *Journal of Advances in Modeling Earth Systems* **11**, 998–1038 (2019).

[85] Seland, Ø. *et al.* Overview of the norwegian earth system model (noresm2) and key climate response of cmip6 deck, historical, and scenario simulations. *Geoscientific Model Development* **13**, 6165–6200 (2020).

[86] Good, S. A., Martin, M. J. & Rayner, N. A. En4: Quality controlled ocean temperature and salinity profiles and monthly objective analyses with uncertainty estimates. *Journal of Geophysical Research: Oceans* **118**, 6704–6716 (2013).

[87] Gouretski, V. & Reseghetti, F. On depth and temperature biases in bathythermograph data: Development of a new correction scheme based on analysis of a global ocean database. *Deep Sea Research Part I: Oceanographic Research Papers* **57**, 812–833 (2010).

[88] Levitus, S. *et al.* Global ocean heat content 1955–2008 in light of recently revealed instrumentation problems. *Geophysical Research Letters* **36** (2009).

[89] Cowley, R., Wijffels, S., Cheng, L., Boyer, T. & Kizu, S. Biases in expendable bathythermograph data: A new view based on historical side-by-side comparisons. *Journal of Atmospheric and Oceanic Technology* **30**, 1195–1225 (2013).

[90] Cheng, L., Zhu, J., Cowley, R., Boyer, T. & Wijffels, S. Time, probe type, and temperature variable bias corrections to historical expendable bathythermograph observations. *Journal of Atmospheric and Oceanic Technology* **31**, 1793–1825 (2014).

[91] IOC, SCOR & IAPSO. *The international thermodynamic equation of seawater - 2010: Calculation and use of thermodynamic properties. Intergovernmental Oceanographic Commission, Manuals and Guides No. 56, UNESCO (English), 196 pp* (2010). URL https://www.teos-10.org/.

[92] Schulzweida, U. Cdo user guide (2023).

[93] Moat, B. I. *et al.* Atlantic meridional overturning circulation observed by the RAPID-MOCHA-WBTS (RAPID-Meridional Overturning Circulation and Heatflux Array-Western Boundary Time Series) array at 26N from 2004 to 2024 (v2024.1a) (2026).

Funding Declaration

This research was supported by the ASPECT project, which has received funding from the European Union's Horizon Europe research and innovation programme under grant agreement No 101081460. Views and opinions expressed are, however, those of the author(s) only and do not necessarily reflect those of the European Union. Neither the European Union nor the granting authority can be held responsible for them.

DG, DN, and PJA received funding from the ASPECT project, under the European Union's Horizon Europe—the Framework Programme for Research and Innovation (2021–2027), Grant Agreement No. 101081460.

DMS received funding from the Met Office Hadley Centre Climate Programme funded by Department for Business, Energy and Industrial Strategy (BEIS) and Department for Environment, Food & Rural Affairs (Defra), ASPECT (grant no. 101081460) and EXPECT (grant no. 101137656) projects.

DMWF received funding from a Laura Bassi Fellowship from the Euro-Mediterranean Center on Climate Change (CMCC).

Author Contributions

D.G., D.N., and P.J.A. conceived and designed the study. D.G. led the work, with material preparation, data collection and formal analysis. All authors contributed to the interpretation of the results through scientific discussions and provided valuable ideas and critical feedback. D.G. wrote the first draft of the manuscript, and all authors contributed to subsequent revisions. All authors read and approved the final manuscript.

Competing interests

All authors declare no financial or non-financial competing interests.

Additional information

Supplementary information For supplementary information, please see the Supplementary Material.

Correspondence and requests for materials should be addressed to Domenico Giaquinto.

Supplementary Files

This is a list of supplementary files associated with this preprint. Click to download.

- Supplementary.pdf